Journal of the Indian Society of Remote Sensing (January 2024) 52(1):95–111
https://doi.org/10.1007/s12524-023-01805-x

RESEARCH ARTICLE

Hydrometeors Distribution in Intense Precipitating Cloud Cells Over the Earth's During Two Rainfall Seasons

Shailendra Kumar[1] · Jose Luis Flores-Rojas[2] · Aldo S. Moya-Álvarez[2] · Daniel Martínez-Castro[2] · Yamina Silva[2]

Received: 3 November 2022 / Accepted: 16 December 2023 / Published online: 25 January 2024

Abstract

In the present study, we used attenuated corrected radar reflectivity factor (Z_e) and rain-drop size distribution (DSD) to investigate the hydrometeors distribution in the intense precipitating cloud cells (PCCs) from precipitation radar (PR) onboard on Global Precipitation Measurement (GPM). The DSD parameters consist of two variables, namely, mass-weighted mean diameter (D_m) in mm and normalized scaling parameters for hydrometeors concentration (N_w) in mm^{-1} m^{-3}. We defined two types of PCCs, which are the proxies for the intense rainfall events. First PCC is termed as Cumulonimbus Towers (CbTs), which consist of $Z_e >= 20$ dBZ at 12 km altitude, and its base height must be less than 3 km altitude. We also defined intense convective clouds (ICCs), which consist of $Z_e > 30$ (40) dBZ at 8 km (3 km), respectively, and are termed as ICC8 and ICC3, respectively. The spatial distribution reveals that continental areas consist of a higher frequency of CbTs and ICC8s compared to oceanic areas, whereas ICC3s are uniformly distributed over tropical land and oceanic areas. The DSD parameters reveal that intense PCCs have larger hydrometeors (D_m), whereas weaker (less Z_e) vertical profiles consist of higher concentration (N_w) of smaller hydrometeors (D_m). Land consists of larger hydrometeors (D_m) compared to oceanic areas, and differences are higher in liquid phase regimes compared to mixed phase regimes. The vertical profiles of Z_e, D_m and N_w are showing the higher regional differences among the different land-based areas, compared to various tropical ocean basins. Western Himalaya Foothills and Sierra De Cordoba consist of the strongest vertical profiles with the largest D_m on the Earth's areas during JJAS and DJFM months, respectively.

Keywords GPM · Precipitation radar · Orography · Radar reflectivity factor · DSD parameters

Introduction

Meso-scale convective systems (MCSs) are the major source of the surface precipitation on Earth (Houze, 2012; Liu & Zipser, 2015; Kumar et al., 2019a). Cumulonimbus (Cb) clouds are the building blocks of these MCSs (Houze, 1993) and transport moisture and energy from the atmosphere's lowest level to the upper atmosphere (e.g., Riehl & Malkus, 1958). Precipitation radar (PR) onboard the TRMM (Tropical Rainfall Measuring Mission) and GPM (Global Precipitation Measurement) provides the three-dimensional structure of the precipitation from space. They primary observed variable is the attenuated corrected radar reflectivity factor (Z_e) which are used to extract the several precipitations characteristics such as their size, intensity, variability, diurnal cycle and life cycle properties over the tropics (Peterson & Rutledge, 2001; Takayabu, 2002; Nesbitt et al., 2000, 2006; Hirose & Nakamura, 2005; Xu & Zipser, 2012; Wu et al. 2013, 2016; Nesbitt et al., 2006; Zipser et al., 2006; Houze et al., 2007; Liu et al., 2008; Romatschke et al., 2010; Xu & Zipser, 2012; Kumar, 2016; 2017a; Kumar & Bhat, 2017, 2019; Wu et al., 2020; Kumar et al., 2019b; 2020a).

The vertical variations of Z_e in cloud systems depend on the geographical locations, and tropical continental clouds have higher Z_e compared to oceanic and mid-latitude cloud systems (Xu & Zipser, 2012; Zipser & Lutz, 1994). Peterson and Rutledge (2001) used the PR-based measured Z_e for the precipitation cloud population and observed that land-based precipitation is more convective in nature, and they are deeper compared to oceanic ones. Liu et al. (2008) studied the relationship between lightning flash rate and Z_e

✉ Shailendra Kumar
shailendrak89@gmail.com

[1] Space Physics Laboratory, Vikram Sarabhai Space Research Centre, Indian Space Research Organization, Trivandrum, Kerala 695022, India

[2] Institute of Geophysics, 15012 Lima, Peru

in the thunderstorms over the tropics and subtropics. Qie et al. (2014) observed the most frequent deep and intense convection over the westmost part of the southern Himalayan front with a higher echo top of 40 dBZ compared to the Tibetan Plateau, which has relatively weaker convective intensity and smaller convective systems. A higher of Z_e in the precipitating cloud systems in the upper troposphere reflects the lightning activity in the cloud systems (Yuan & Qie, 2008). Xu and Zipser (2012) also investigated the precipitating cloud systems over various tropical areas. They observed that cloud depth is strongly correlated with the updraft velocity in the mixed phase altitude within the clouds. Bhat and Kumar (2015) investigated the Cb clouds using the TRMM PR data and showed that land-dominated regions show the higher regional differences among themselves in the mixed phase altitude. However, over oceanic basins the major differences in Cb clouds are observed in their frequency rather than their vertical profiles (Kumar & Bhat, 2016). However, the climatological rain-drop size distribution (DSD) distributions are not reported earlier over the specific locations and on regional and seasonal basis due to the unavailability of data. It leaves the uncertainty in their representation in the regional and climate models which could reveal the growth mechanism within the Cb clouds.

Ground-based vertical profiler radar showed that vertical variation in DSD parameters depends on the rainfall rate (Das and Maitra, 2016; Lavanya et al., 2019 ; Kumar et al., 2020b; Del Castillo-Velarde et al., 2022). The climatological knowledge about DSD parameters over specific locations will improve their representation in the climate models (Xu & Zipser, 2012), which are the biggest source of uncertainty in the climate models. The main objectives are here:

(a) Where do the most intense precipitating cloud cells occur over the Earth's (60°S to 60°N) using 7 (2014–2021) years of GPM data?
(b) How do the precipitation-related parameters such as Z_e, and DSD parameters vary vertically over different parts of the Earth during two monsoon seasons, namely, June to September (JJAS months, summer monsoon) and December to March (DJFM months, winter season)?
(c) To know the differences in the vertical structure of convective clouds that form under different climatic conditions?

Data and Methodology

To strengthen the measurement from the atmosphere, the National Institute of Communication Technology (NICT) and the Japan Aerospace Exploration Agency (JAXA) launched GPM in February 2014. GPM consists of a dual-PR (DPR) which works at two frequencies (K_u-PR, 13.6 GHz) and (K_a-PR, 35.5 GHz). It provides the three-dimensional field of Z_e (in dBZ) and DSD parameters along the globe. DSD parameters consist of two variables, namely normalized scaling parameters for hydrometeors concentration (N_w in mm^{-1} m^{-3}) and mass-weighted mean diameter (D_m in mm). The spatial coverage of DPR lies between 65°S and 65°N and monitors the globe nearly 15–16 times in a day with a swath width of ~ 250 km. The Ku-PR uses the 49 PR beams with a beam width of 0.71°. The maximum scanning angle for the extreme beams (1st and 49th PR beam) is 17° from the zenith beam (25th beam). The sensitivity of GPM-PR is 14 dBZ (Hamada & Takayabu, 2016) with measurement accuracy within 1 dBZ (Hou et al., 2014). Data from European Centre for Medium-Range Weather Forecasts (ECMWF; Dee et al., 2011) and National Centers for Environmental Prediction (NCEP; Kalaney et al., 1996) for sea surface temperature (SST), convective available potential energy (CAPE), temperature (T), specific humidity (q), geopotential height (hgt) and moist static energy (MSE) are also used to investigate the atmospheric conditions during study periods.

To investigate the hydrometeors distribution in the intense precipitating cloud cells (PCCs), two types of PCCs are defined and mentioned below.

(a) Cumulonimbus Towers (CbTs): CbTs consist of $Z_e >= 20$ dBZ at 12 km altitude, with a base height of less than 3 km and atleast 9 km thick (Bhat & Kumar, 2015).
(b) ICC based on 3 km (ICC3) and 8 km (ICC8): ICCs are defined by considering a fixed Z_e threshold, e.g., 40 and 30 dBZ at the 3 and 8 km, respectively (Kumar & Silva, 2019, 2020).

The 3 km altitude lies well below the freezing height (~ 5 km, FH, °C), and most of the hydrometeors will be liquid phase only, where hydrometeors size and concentration will be the results of collision-coalescence microphysical processes (Houze, 1993, 2012). The reduction in the hydrometeors size below the FH will be the result of evaporation and breakup (Das and Maitra, 2016; Kumar & Srivastava, 2022) in the dry weather. The 8 km altitude is well above the FH, and most of the hydrometeors will be in the frozen or supercooled state, and they are the results from different cold microphysical processes (Houze, 1993).

To derive the intense PCCs from the 3-dimensional field of Z_e a well-defined algorithm, namely VPRR (vertical profile of radar reflectivity), is used (Zipser & Lutz, 1994). First, for each satellite pass maximum Z_e (MAX-Z_e) is observed at the mentioned altitude (3, 8 and 12 km). If MAX-Z_e is higher than the threshold Z_e at each mentioned altitude (40, 30 and 20 dBZ), we constructed an intense PCC. A PCC is formed by selecting the maximum Z_e from the 9 GPM-DPR beams, e.g., one beam which has the maximum Z_e and its 8 neighbor eight beams. After constructing the PCC, the values of 9 GPM-DPR beams are set to zero. This process is repeated again and again, and once MAX-Z_e is less than the defined thresholds, the process is stopped (Fig. 1).

The physical significance of the derived PCCs can be understood by considering the life cycle of the clouds. At the initial phase of Cb clouds updraft speed remains very high, which takes the hydrometeors at the upper altitude due to strong convective activity. As the Cb clouds mature, the updraft speed weakens, and hydrometeors start falling downward. As they reach to lower altitude, ice microphysical processes (riming & aggregation) increase their size. Because of increase in the size, the Z_e increases and the highest Z_e is observed in the mature phase (Kumar & Bhat 2019; Fabry & Zawadaki, 1995; Kumar & Srivastava, 2022; Kumar et al., 2020a, 2020b, 2020c; Williams et al., 1989). In the dissipating phase the *Ze* has the least values at higher altitude, but lies between the initial and mature phase below 6 km altitude (Kumar & Srivastava, 2022).

Figure 2 shows a vertical cross section of Z_e for a GPM pass on January 10, 2016, over central India. It is observed that PCC 'C' has higher Z_e in the upper troposphere compared to PCCs 'F' and 'G.' However, PCCs 'F' and 'G' have much higher Z_e in the lower troposphere, especially between 2 and 5 km altitude, and we can assume them at mature and later phases of Cb clouds. In the tropical atmosphere, 8 km lies in the mixed phase altitude (Stith et al., 2002) and both

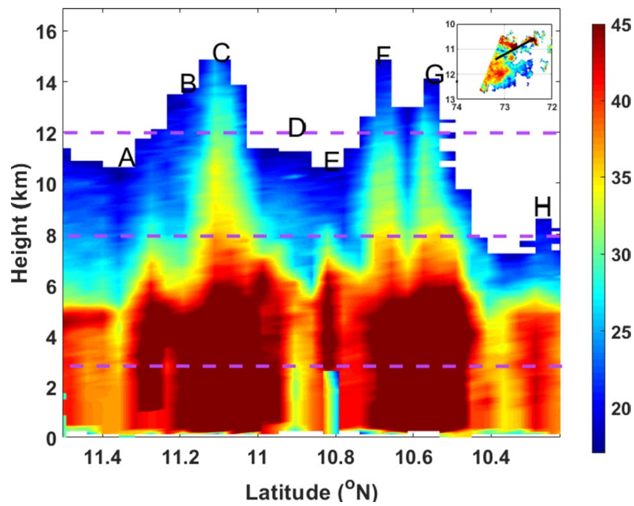

Fig. 2 An example vertical cross-selection for a cloud system observed over central Indian region on January 10, 2016. The inset shows a horizontal section taken at 3.5 km altitude (the abscissa and ordinate are longitude and latitude, respectively). The vertical section is taken along the lines that cut through active convective clouds and is plotted against latitude. The color bar on the right shows Ze (dBZ) (color figure online)

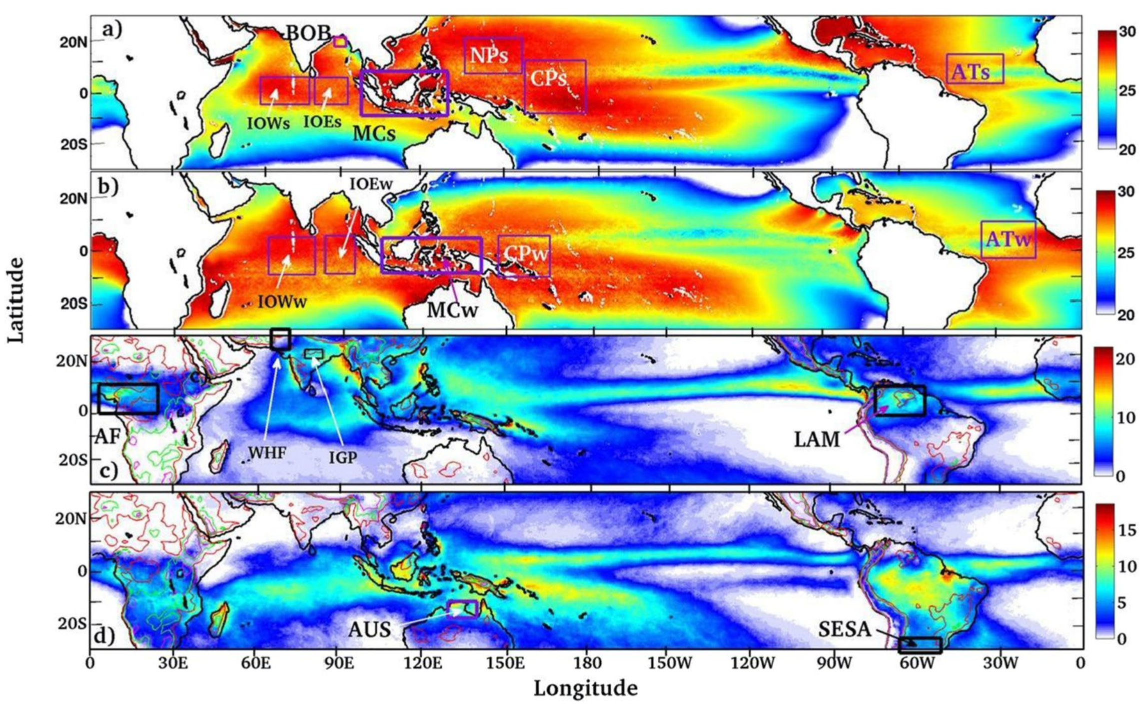

Fig. 1 Seasonal-average TMI SST and TRMM 3B42 precipitation for the 17-yr period from 2001 to 2017: **a** SST for June–September, **b** SST for December–March, **c** June–September daily average precipitation and **d** December–March daily average precipitation. Color bars on the right show SST (°C) or precipitation (mm day^{-1}). Areas selected for detailed analysis are shown by rectangular boxes. See Table 1 for their description (color figure online)

convective and stratiform precipitation contribute to rainy pixels (Li & Schumacher, 2011). Thus we can assume that CbTs, ICC8s and ICC3s are providing precipitation information from the different phases of the life cycle of Cb clouds.

Results

Global Distribution of CbTs and ICCs During JJAS and DJFM Months

Figure 3 shows the spatial distribution of three different types of PCCs in $1^\circ \times 1^\circ$ grid boxes during the JJAS and DJFM months. Northern and southern hemisphere consists of a higher frequency of PCCs, during summer (JJAS) and winter (DJFM) seasons, respectively (Fig. 3d; Liu & Zipser, 2015; Kumar et al., 2019a). The spatial distribution of CbTs (Fig. 3a, b) and ICC3s (Fig. 3e, f) follows the tropical rainfall climatology (Fig. 1) over tropical and subtropical latitudes. The ICC8s are mostly observed over the tropical and subtropical land areas (Fig. 3c), and oceanic areas do not have a significant frequency of ICC8s. During JJAS months, higher number/frequency of CbTs and ICC8s are observed over the Indo-Gangetic Plain (IGP), north-central Africa (AF), Costa-Rica, Maritime Continent (MC), central-south USA and northern South America (SA) (Fig. 3a, b; Liu & Zipser, 2015). However, during DJFM months, the higher frequency of CbTs and ICC8s is shifted in the southern hemisphere (Fig. 3d, e) and number/frequency of CbTs is higher over the SA continent, central AF, MC and northern Australia (AUS).

Land vs ocean contrast and seasonal differences are least in ICC3s where both land and ocean areas consist of a comparable number of ICC3s (Fig. 3c & f). In JJAS months, oceanic areas such as the Bay of Bengal (BOB), east Pacific Ocean (PO) and Atlantic Ocean (AO) have a higher number frequency of ICC3s within the tropical belt (Fig. 3e). Land-dominated regions such as northeast India, IGP, Western Ghats (WG), MC, central AF, Brazilian Highlands and Mexico consist of higher frequency of ICC3s (Fig. 3e). During DJFM months, oceanic areas such as tropical west PO and tropical AO with subtropical PO, along with land-dominated areas over central-south AF, MC, northern AUS and continental SA, consist of higher frequency of ICC3s (Fig. 3f). The least differences between land and ocean in ICC3s reveal that convection over land and ocean is able to produce uniform shallow precipitation over the tropics and subtropics (Xu & Zipser, 2012; Kumar, 2018; Wu et al., 2020).

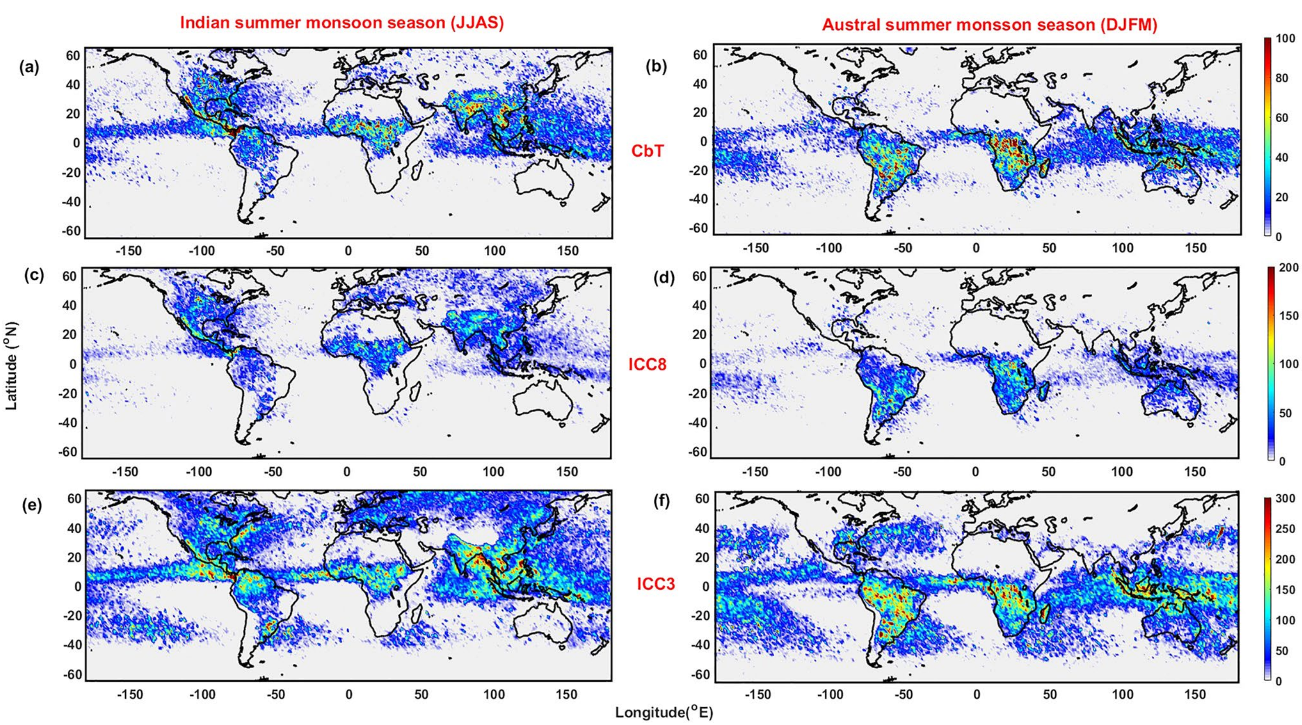

Fig. 3 Spatial distribution of cloud cells in each $1^\circ \times 1^\circ$ grid box during Indian (JJAS) and Austral summer (DJFM) monsoon for the year between December 2014 and December 2021. The color bar shows the number of each type of intense precipitating cloud cells (color figure online)

Vertical Distribution of Radar Reflectivity in CbTs and ICCs

The present study also explored the regional differences in the PCCs vertical profiles among 18 areas (Table 1). The boxes are selected based on SST, rainfall patterns and past studies (Fig. 1; Xu & Zipser, 2012; Zipser et al., 2006). Figure 4 shows the mean Z_e vertical profiles for the PCCs over the selected areas. The mean vertical profiles show the opposite variation below and above the FH, and the peaks in average Z_e are observed near 4–5 km height. For example, above the FH, Z_e decreases with the altitude, but below the FH either they increase, decrease or remain constant depending on the geographical locations. The regional differences in mean Z_e are less than 2–3 dBZ among the selected areas below the FH (Kumar 2023). Regional differences are higher among the land-based PCCs compared to oceanic-based PCCs and observed in the earlier studies too (2017b; Kumar & Bhat, 2016; Lucas et al., 1994; Xu & Zipser, 2012; Zipser & Lutz, 1994; Zipser et al., 2006). Average vertical profiles are showing the higher regional differences between 6 and 9 km altitude and reveal that mixed phase altitude must be investigated extensively to investigate the differences in the ocean and land-based intense PCCs (Lasher-Trapp et al., 2018).

The regional differences are highest in CbTs followed by ICC3s among the selected areas, whereas land–ocean differences are least in ICC8s (Fig. 4a–c). Western Himalaya Foothills (WHF) and Sierra de Córdoba (SDC) consist of the most intense PCCs during JJAS and DJFM months, respectively (Zipser et al., 2006; Kumar & Silva, 2019, 2020; Kumar et al., 2023). Among the land-dominated areas the intensity is decreasing in the order of WHF, SDC, IGP, AF and LAM and AUS in mixed phase and upper-level altitude (in the layer between 5 and 10 km, Fig. 4a). BOB and MC show nearly identical behavior, and their average *Ze* vertical profiles lie between continental and oceanic regions. The behavior is because of their selection, as both the selected regions are very near to landmass and may be the land area is influencing the vertical characteristics. The Atlantic Ocean (AO) and Equatorial Indian Ocean (IOEs) consist of the weakest (less *Ze*) vertical profiles among the selected oceanic areas (Fig. 4b).

Distribution of Echo Top Height

A box plot of the maximum height of 20 dBZ (MH20) is shown in Fig. 5 and also tabulated in Table 1. It can also be considered as an echo top height (ETH, Kumar, 2017a). Median and average ETHs are marked in red lines (bars) and green dots, respectively, whereas box edges represent the 75 and 25 percentiles of ETHs. Land-based PCCs are showing higher average and median ETHs compared to oceanic-based PCCs. Regional differences are showing similar characteristics among the selected areas for different types of PCCs. WHF and IGP have the highest median ETH (> 14.500 km) during JJAS months in CbTs, whereas AUS (> 14.125 km) has the highest median ETH during DJFM months. The Indian Ocean (< 13.000 km) and Atlantic Ocean (12.375 < km) have the least ETH during both the seasons. ICC3s also shows the similar features, and WHF & IGP and SDC have the highest median and average ETH during JJAS and DJFM months, respectively. Again, the Indian and Atlantic Ocean have the least ETH during both the seasons. ICC8s show different characteristics, and AF & LAM and AUS have the highest median ETH during JJAS and DJFM months, respectively.

Table 1 shows the median height of the maximum height of 30 and 40 dBZ (MH30 & MH40). It is clear that PCCs are deeper over the land compared to oceanic areas. Again, WHF has the highest MH30 (12.500 km, 10.500 km and 8.875 km in CbTs, ICC8s and ICC3s, respectively) and MH40 (8.500, 8.000, 6.625 km in CbTs, ICC8s and ICC3s, respectively) during JJAS months. In DJFM months SDC (R-18) has the highest MH30 (12.125 km, 10.375 km and 7.875 km in CbTs, ICC8s and ICC3s, respectively) and MH40 (9.375 km, 10.500 km and 5.500 km in CbTs, ICC8s an ICC3s, respectively), respectively. Among the oceanic-dominated areas, MC and BOB have higher MH30 and MH40 and these areas are very near to land. Among the tropical oceans, AO has the minimum MH30 and MH40 during both the seasons.

Spatial Variation in DSD Parameters

Figures 6 and 7 are showing the spatial distribution of D_m (in mm) for PCSs in each $1° \times 1°$ grid box at 3 and 8 km altitude, respectively. Figures 8 and 9 are showing the spatial distribution of N_w (in mm^{-1} m^{-3}) for PCCs in each $1° \times 1°$ grid box at 3 and 8 km altitudes, respectively. At 3 km altitude, hydrometers (D_m) are larger compared to 8 km altitude both over land and oceans, and land and oceanic differences are higher at 3 km compared to 8 km altitude. For example, land-dominated areas have higher concentrations of larger D_m (> 3.5 mm and 2 mm at 3 km and 8 km). Oceanic PCCs have a higher concentration of N_w (> 35 mm^{-1} m^{-3}) of small size of D_m (< 1.5 mm) at 8 km altitude. The corresponding value at 3 km is 30 mm^{-1} m^{-3} and D_m is less than 2 mm. Land and ocean differences may be associated with the updraft velocity over land and oceanic areas, which is higher over the land (Heymsfield et al., 2010; Zipser & Lutz, 1994) and takes the hydrometeors at higher altitudes.

During JJAS months, CbTs over western India (WHF and WG), central AF, land masses of SA and USA consist of the largest hydrometeors (D_m > 4 mm) at 3 km altitude. The tropical oceanic areas consist of small-sized

Table 1 Median height for maximum height of 20, 30 and 40 dBZ over the selected areas for different types of cloud cell

No	Height thresholds	CbT			ICC8			ICC3		
	Boundary	MH20	MH30	MH40	MH20	MH30	MH40	MH20	MH30	MH40
1	Bay of Bengal (BOB) (86°E–93°E, 15°N–20°N)	14.000	9.625	6.375	12.500	9.250	6.375	9.375	6.750	5.375
2	Indian Ocean west (IOWs) (55°E–79°E, 5°S–3°N)	13.500	8.750	5.500	13.125	9.125	5.625	9.000	6.000	4.750
3	Indian Ocean east (IOEs) (81°E–100°E, 5°S–3°N)	13.500	9.125	5.750	13.000	9.125	5.875	8.875	6.125	4.750
4	Maritime continent (MCs) (105°E–130°E, 9°S–10°N)	13.875	10.2500	6.125	13.125	9.625	6.250	9.375	6.625	5.000
5	North Pacific (NPs) (135°E–155°E, 5°S–20°N)	13.875	8.750	5.625	13.500	9.250	5.875	9.875	6.625	5.125
6	Central Pacific (CPs) (156°E–180°E, 15°S–5°N, 180°W–170°W, 15°S–5°N)	13.750	8.625	5.625	13.375	9.125	5.750	9.625	6.500	5.000
7	Atlantic Ocean (ATs) (50°W–20°W, 0–10°N)	13.375	7.750	5.375	13.375	9.125	5.625	9.125	5.875	4.75
8	Western Himalaya foothills (WHF) (65°E–72°E, 28°N–33°N)	14.500	12.500	8.500	12.125	10.500	8.000	11.125	8.875	6.625
9	Indo-Gangetic plain (IGP) (76°E–86°E, 21°N–36°N)	14.625	11.375	7.500	12.750	9.875	7.625	10.625	8.000	5.875
10	Africa (AF) (4°E–28°E, 0–10°N)	14.250	11.500	7.000	13.500	10.750	7.000	10.500	7.500	5.500
11	Latin America (LAM) (75°W–50°W, 10°S–2°N)	14.125	11.125	6.500	13.625	10.625	6.750	9.125	6.625	5.000
12	Indian Ocean East (IOEw) (55°E–79°E, 10°S–2°N)	12.375	9.750	6.125	12.750	8.750	5.625	8.625	6.000	4.750
13	Indian Ocean West (IOWw) (87°E–95°E, 11°S–20°N)	12.625	10.125	6.500	13.000	9.125	6.000	8.625	6.125	4.875
14	Maritime Continent (MCw) (110°E–140°E, 0–12°N)	13.750	8.750	5.875	13.000	9.125	6.125	9.375	6.500	5.125
15	Centre Pacific Ocean (CPw) (145°E–170°E,11°S–2°N)	13.625	8.375	5.750	13.000	8.875	6.000	9.375	6.375	5.125
16	Atlantic Ocean (ATw) (30°W–10°W, 3°S–7°N)	13.125	8.875	5.875	12.500	9.125	6.125	8.750	6.125	4.875
17	Australia (AUS) (132°E–145°E, 18°S–10°S)	14.125	9.875	6.375	13.500	9.750	6.375	9.875	6.875	5.375
18	Sierra de Cordoba and La Plata Basin (SDC) (70°W–62°W, 36°S–25°S)	13.500	12.125	9.375	12.000	10.375	8.500	10.125	7.875	5.500

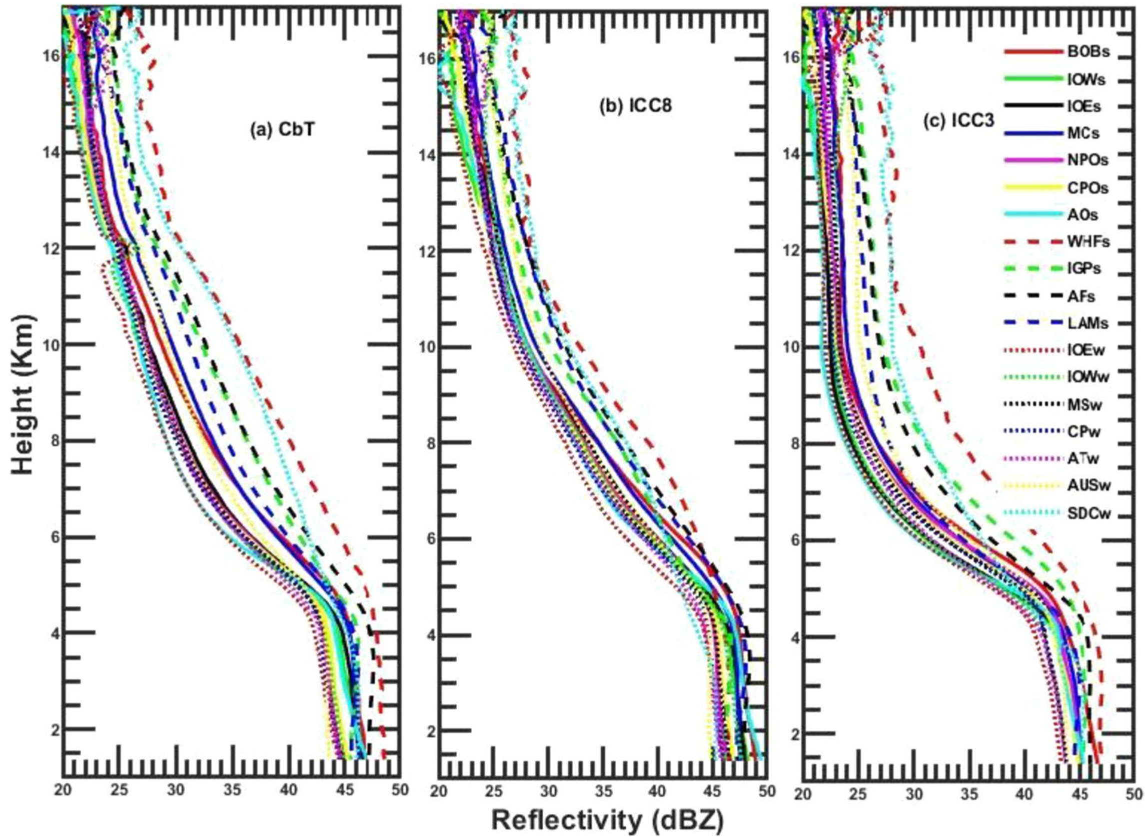

Fig. 4 Average vertical profile of radar reflectivity factor (Z_e) in intense precipitating cloud cells. Data below 1.5 km altitude are omitted because of ground contamination

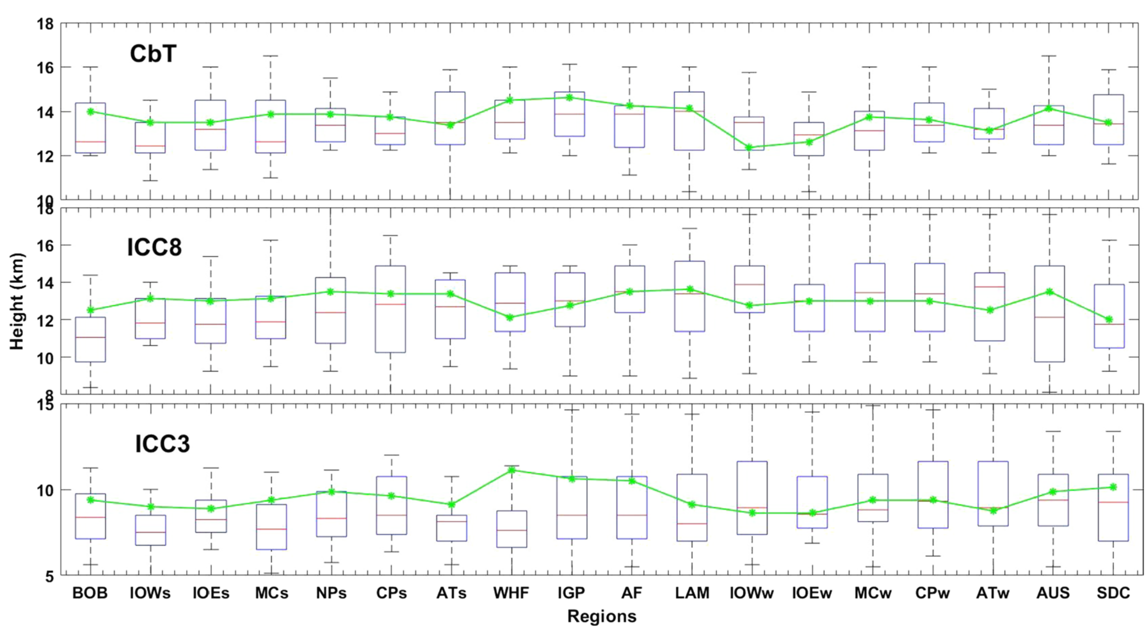

Fig. 5 Maximum height of 20 dBZ in the selected regions

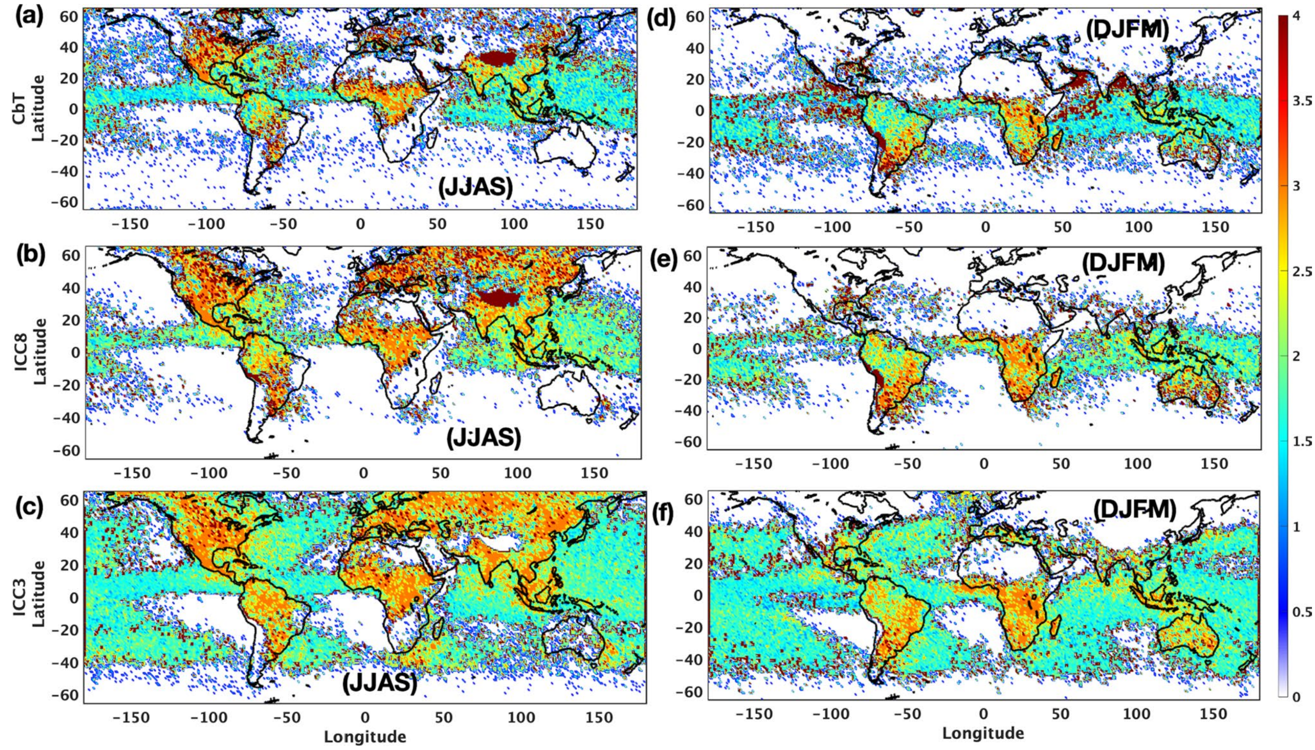

Fig. 6 Spatial distribution of the mean of mass-weighted hydrometeors (D_m) diameters for intense precipitating cloud cells at 3 km altitude, left panels: JJAS months, right panels: DJFM months. The colorbar shows hydrometeors size in mm (color figure online)

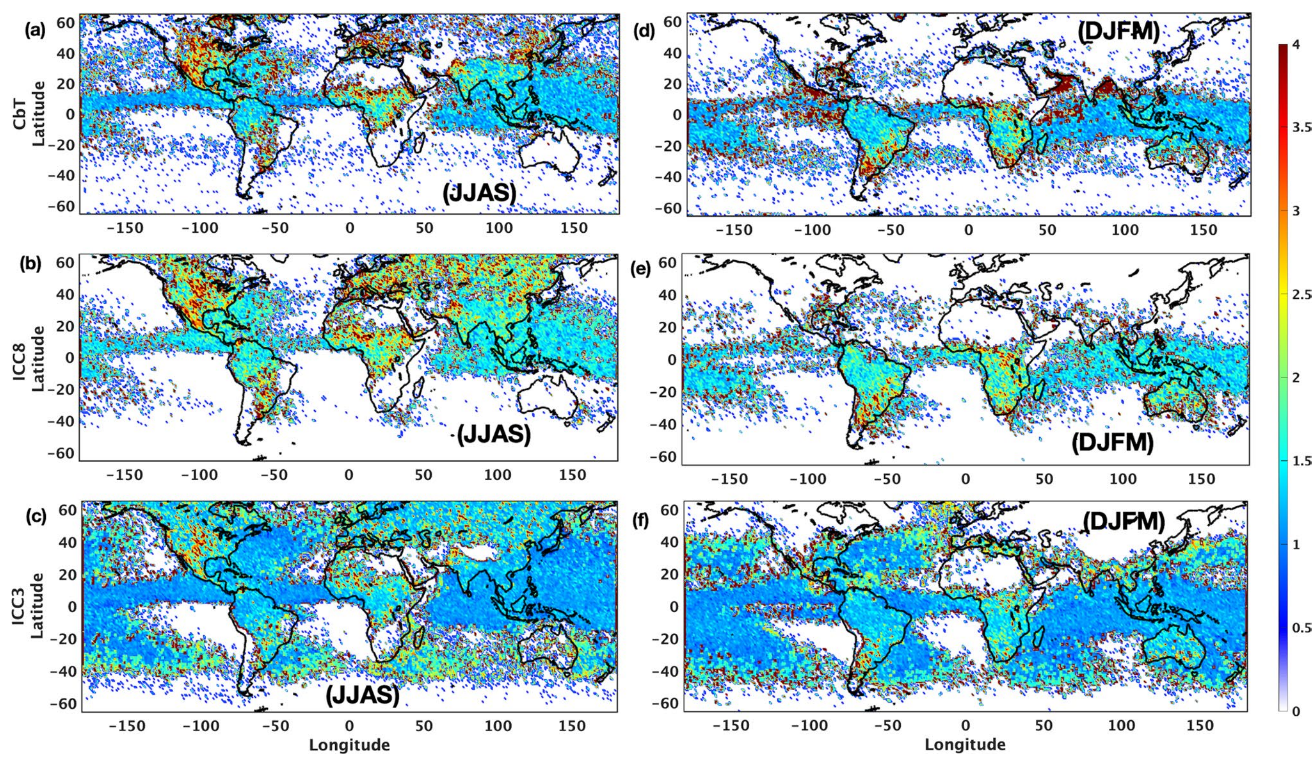

Fig. 7 Spatial distribution of the mean of mass-weighted hydrometeors diameters (D_m) for intense precipitating cloud cells at 8 km altitude, left panels: JJAS months, right panels: DJFM months. The colorbar shows hydrometeors size in mm (color figure online)

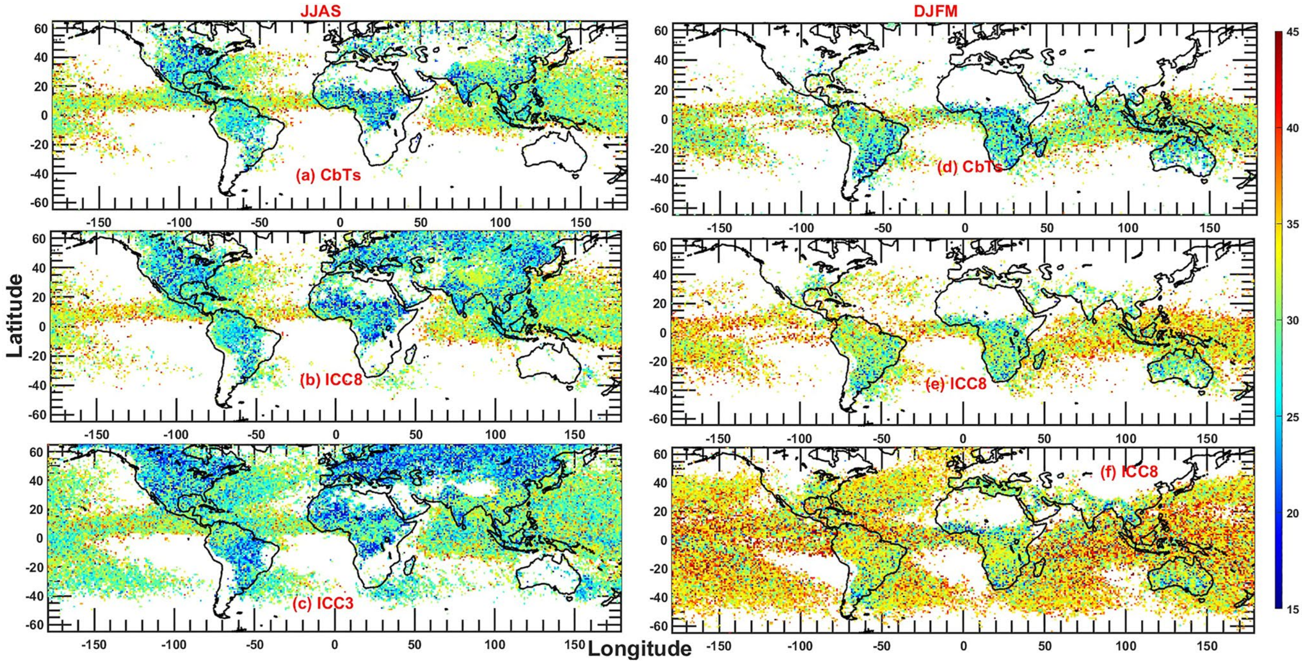

Fig. 8 Spatial distribution of the mean of normal scaling parameters for hydrometeors concentration (N_w) for intense precipitating cloud cells at 3 km altitude, left panels: JJAS months, right panels: DJFM months. The colorbar shows hydrometeors size in mm^{-1} m^{-3} (color figure online)

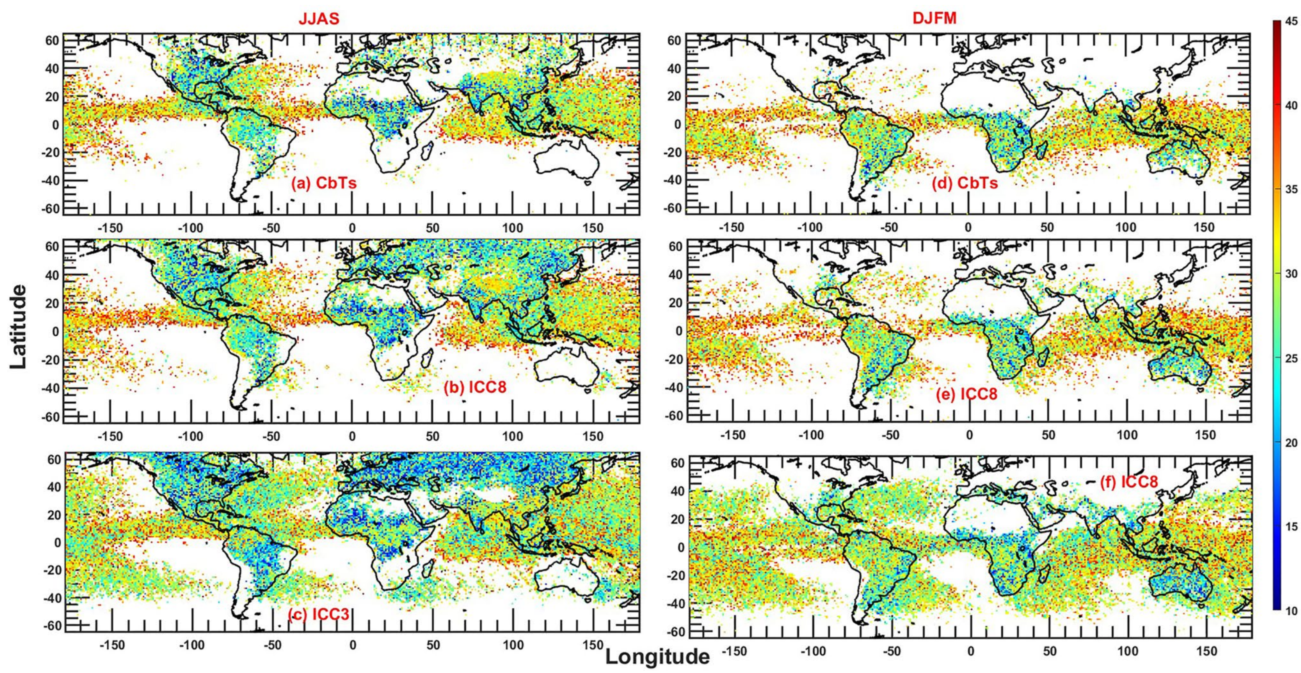

Fig. 9 Spatial distribution of the mean of normal scaling parameters for hydrometeors (N_w) concentration for intense precipitating cloud cells at 8 km altitude, left panels: JJAS months, right panels: DJFM months. The colorbar shows hydrometeors size in mm^{-1} m^{-3} (color figure online)

hydrometeors ($D_m < 2.5$ mm) with higher concentrations (> 40 mm^{-1} m^{-3}) (Fig. 6a). ICC8s show similar characteristics as CbTs have, but regional differences are less over the various land areas compared to CbTs (Fig. 6b). For example, all the tropical land-dominated areas (e.g., India, central AF, north–south SA, subtropical Europe, Russia and USA) consist of larger hydrometeors ($D_m > 4$ mm; Fig. 6b). ICC3s show the least regional differences, and nearly all the landmasses consist of $D_m > 3$ mm compared to oceanic areas ($D_m < 2$ mm; Fig. 6c).

During DJFM months, CbTs have the larger hydrometeors and land masses consist of hydrometeors with $D_m > 4$ mm (Fig. 6d). Again, ICC8s show nearly the similar characteristics as CbTs have and landmass areas such as SA, southern AF, Australia have larger hydrometeors (Fig. 6e). Tropical and subtropical oceans have smaller hydrometers ($D_m < 2$ mm). Figure 6b shows the distribution at an 8 km altitude, and it is observed that there is very less probability that D_m exceeds more than 4 mm in CbTs and ICC8s over land-dominated areas compared to 3 km (Fig. 7a–d). So, there are no comparable regional differences observed between land and ocean. However, D_m in ICC3s does not show the land and ocean differences (Fig. 7c–f) and almost a uniform distribution in D_m is observed, and $D_m < 2 - 1.5$ mm in most of the areas.

Vertical Profiles of DSD Parameters

The median vertical profiles of D_m and N_w are plotted in Figs. 10 and 11 over the selected areas up to 8 km altitude. Like Z_e, DSD also shows the different characteristics below and above the FH and peaks in D_m are observed near 4–5 km altitude (Fig. 10a–c). D_m also decreases above the FH with increasing altitude, but below the FH, D_m either increases, decreases or remains constant depending on the locations. CbTs and ICC8s show the higher regional differences among the land-dominated areas in D_m and N_w compared to oceanic areas. The weaker (less intense) PCCs consist of higher concentration (N_w) of smaller hydrometeors (less D_m), whereas intense PCCs have larger hydrometeors (high D_m) at all PR levels (Fig. 11). Land-dominated areas have a higher concentration (N_w) of larger hydrometeors (D_m) compared to oceanic areas, which consist of higher concentrations (N_w) of smaller hydrometeors (D_m).

D_m values are not exceeding more than 2 mm over tropical oceanic areas, whereas among the land-dominated areas, and north AUS has the smallest hydrometeors (Dm is < 2.5 mm in ICC8s and < 2 mm in CbTs and ICC3s). Overall WHF

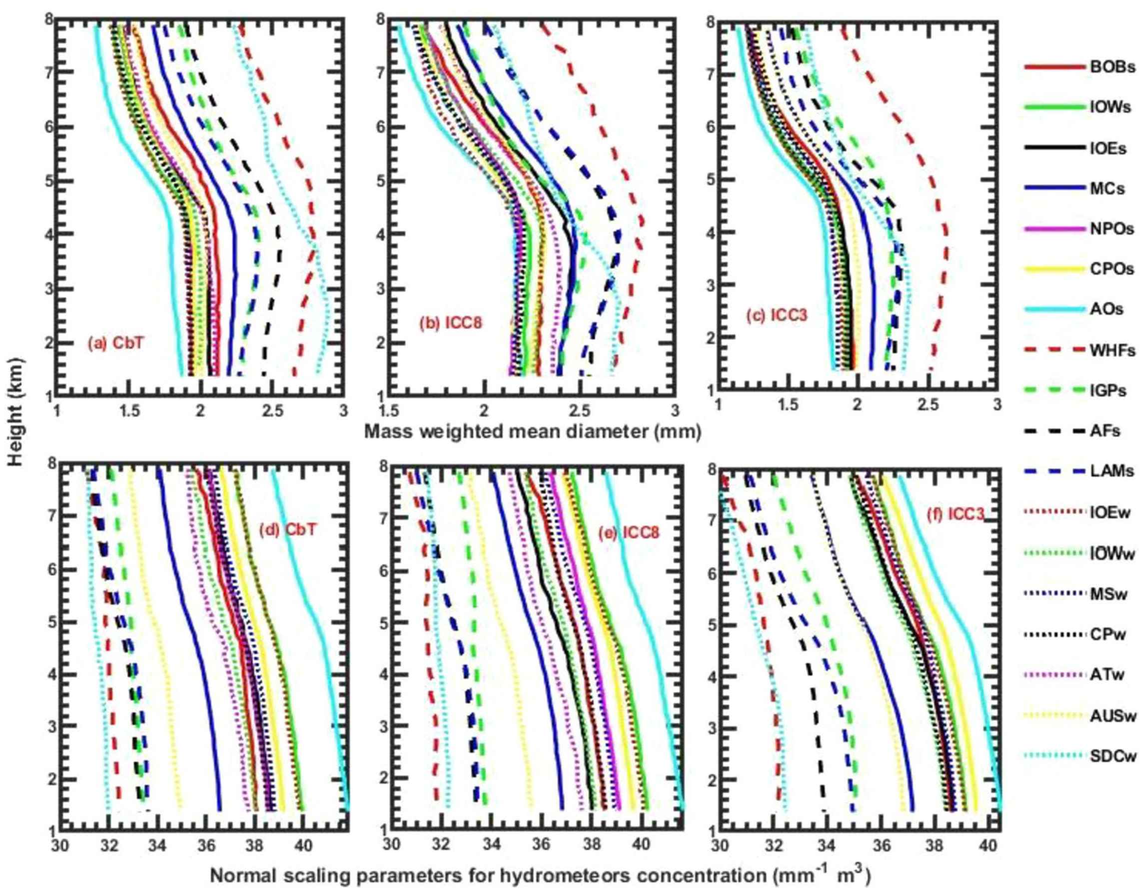

Fig. 10 Average vertical profiles of mass-weighted hydrometeors size (D_m) and normal scaling parameters for hydrometeors concentration (N_w) in cloud cells. Data below 1.5 km altitude are omitted because of ground contamination

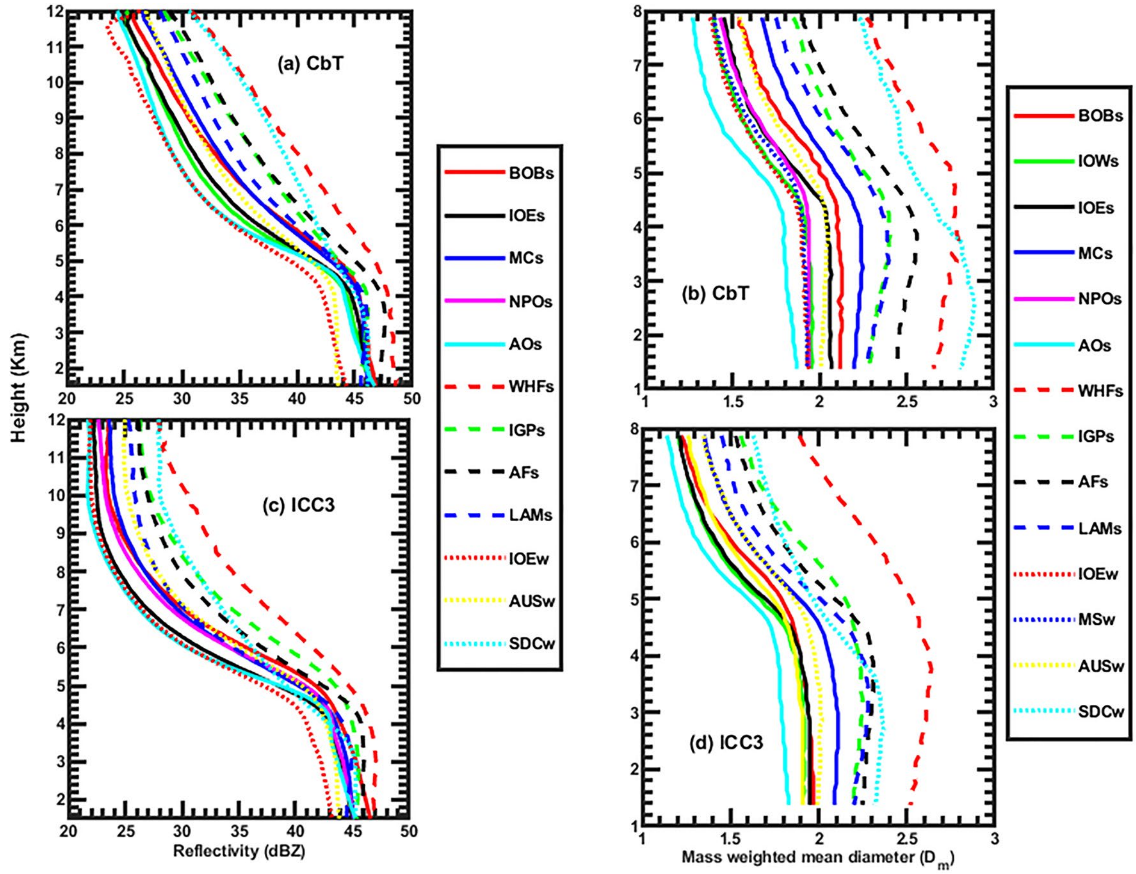

Fig. 11 Average vertical of radar reflectivity and hydrometeors size only over few selected areas to see the proper regional difference. It also shows the relation between intensity (Z_e) and D_m of PCCs

has the highest D_m (> 2.5 mm) at all PR levels (except for the SDC, which has the highest D_m (~ 2.9 mm) below 5 km in CbTs), whereas AO has the least D_m (< 2 mm) at all the PR. This may be associated with higher vertical velocity over land-dominated areas, which lead to the higher size of hydrometeors in the upper atmosphere compared to oceanic areas (Heymsfield et al., 2010; Lucas et al., 1994). The less updraft speed over the oceanic areas leaves the higher concentration of less size of hydrometeors at lower altitudes, which could be removed quickly by shallow precipitation (Lucas et al., 1994). The decreasing order of Dm is nearly identical and only the difference between the Dm over SDC is largest below the 3 km altitude in CbTs. AO has the least Dm in CbTs and ICC3s.

Spatial–Vertical Distribution of D_m in CbTs and ICCs

Figures 12, 13, 14 show the Contoured Frequency by Altitude Diagram (CFAD; Yuter & Houze, 1995) for the D_m in CbTs, ICC8s and ICC3s, respectively. The CFAD diagram shows the spatial–vertical extension of D_m at PR levels. All CFAD's are showing the few important features which are listed below. First, land-based CFADs have higher D_m width at all the altitudes, e.g., land-based PCCs consist of broad D_m spectrum at all the PR levels. Second, land-based CFAD has two maxima (in CbTs) compared to oceanic CFAD, below and above the FH in ICC8s and ICC3s. Third, the modal values are higher (Dm > 2.5 mm) over land-based CFAD compared to oceanic-based CFAD (Dm < 1.3 mm). However, CFAD for ICC3s and ICC8s shows the two maxima, one above and the other below the FH. The maxima below the FH in the land-based PCCs reveal the role of the dominance of collision–coalescence processes, which can increase the hydrometeors size below the 5 km altitude (Cetrone & Houze, 2009). Finally, CbTs (Fig. 12) and ICC8s (Fig. 13) CFAD's width are higher compared to ICC3s (Fig. 14) and represent the higher spectrum width of D_m in the most intense and deepest (CbTs & ICC8s) PCCs compared to shallower and intense PCCs (e.g., ICC3s).

The CFAD diagrams are also showing regional differences. WHF and SDC have the highest CFAD width among all the selected areas and also coincide with the most intense PCCs. They are also showing the highest modal value with D_m > 3.0 mm & > 2.5 mm below the FH. Atlantic Ocean

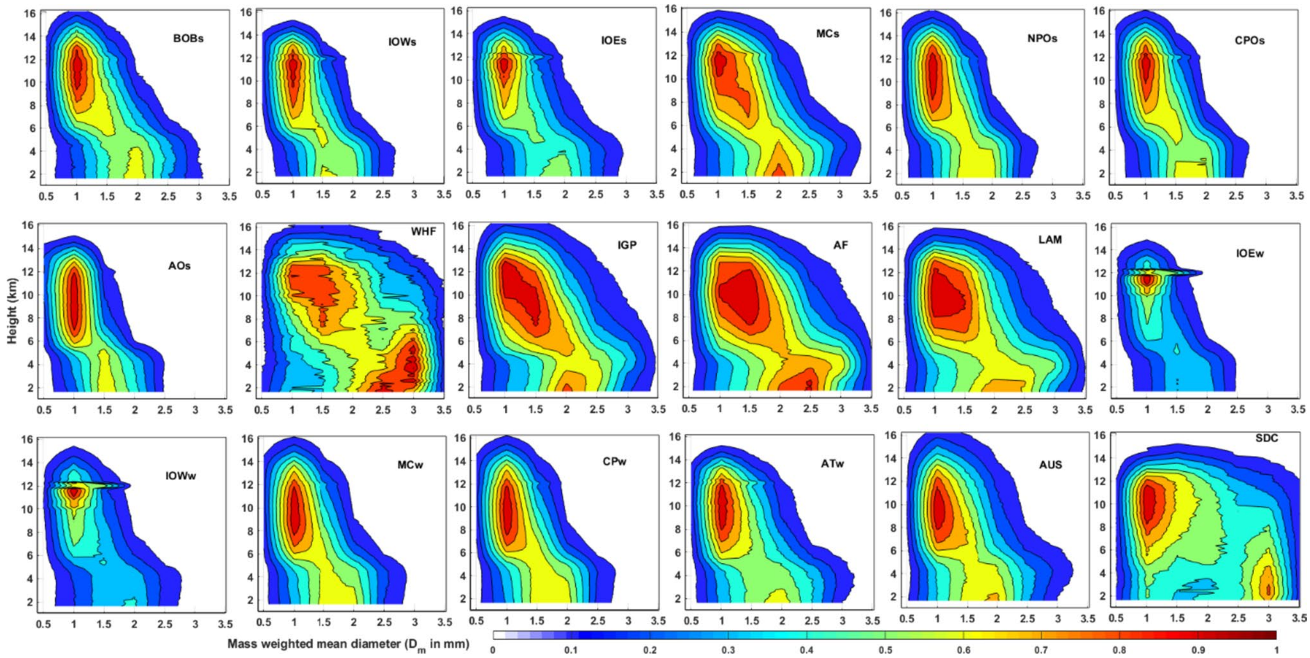

Fig. 12 Contoured frequency by altitude diagram (CFAD) for CbTs in the selected areas. The colorbar indicates the relative occurrences of the D_m at the particular altitude (color figure online)

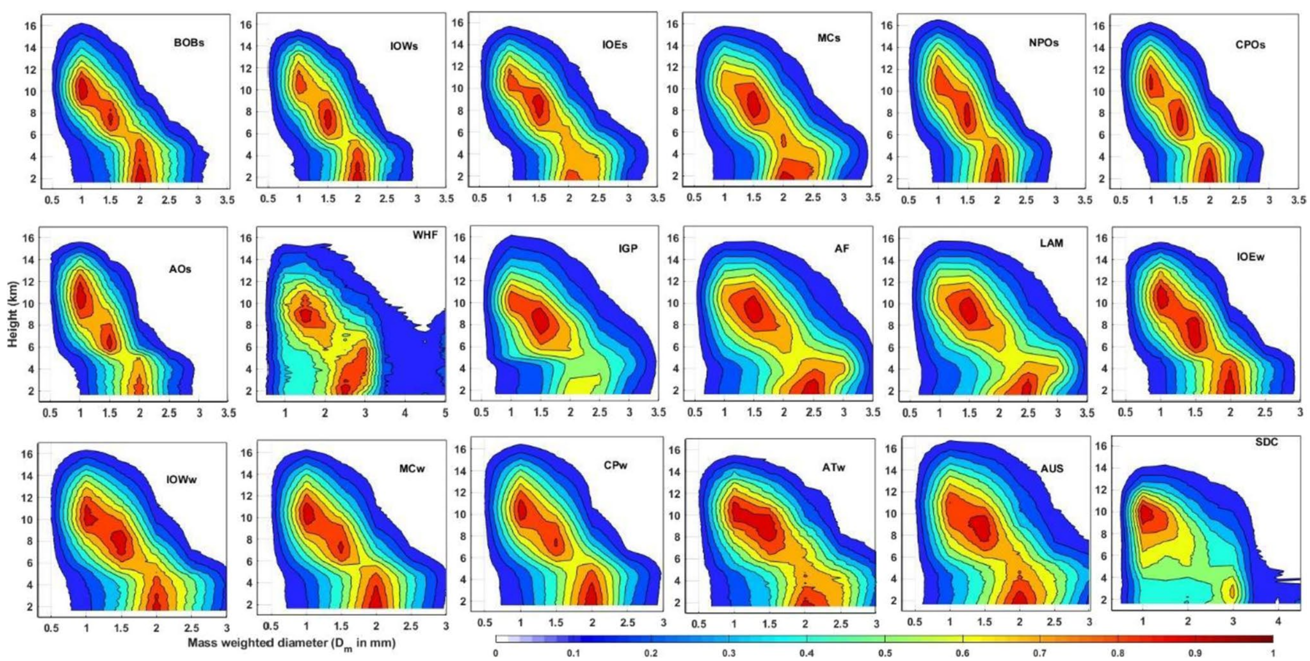

Fig. 13 Contoured frequency by altitude diagram (CFAD) for ICC8s in the selected areas. The colorbar indicates the relative occurrences of the D_m at the particular altitude (color figure online)

(AO) and IOWs have the least CFAD width and correspond to the least intense PCCs. Tropical ocean areas are showing higher modal values ($1 < D_m < 1.5$ mm) only between 9 and 12 km altitude in CbTs compared to land-dominated areas. ICC8's CFAD's are also showing slightly different characteristics compared to CbTs and ICC3s. Although land-based PCCs have higher CFAD width, now both land and ocean-based PCCs are showing the two maxima, one below 5 km altitude and between 9 and 13 km altitude. This indicates that ICC8s are the subset of the strongest CbTs.

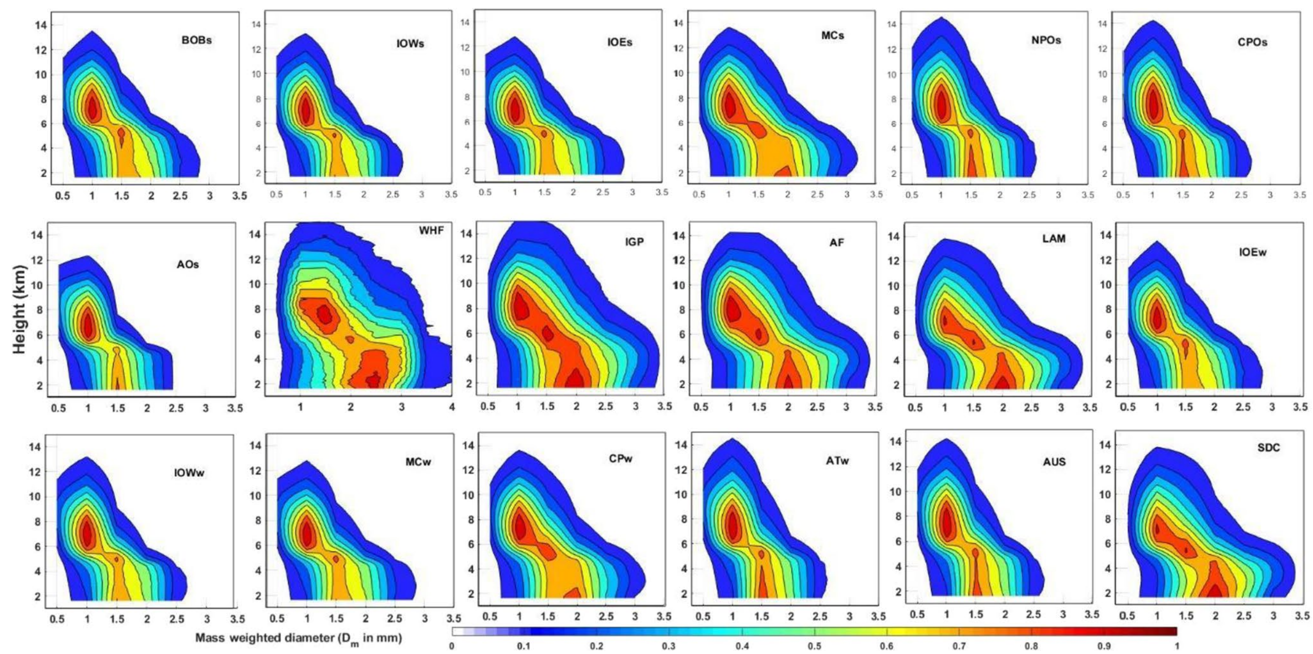

Fig. 14 Contoured frequency by altitude diagram (CFAD) for ICC3s in the selected areas. The colorbar indicates the relative occurrences of the D_m at the particular altitude

Discussion and Conclusions

GPM-PR-based three variables, namely Z_e, D_m and N_w, are used to explore the hydrometeors distribution in the PCCs. It is observed that oceanic-based PCCs consist of close similarity in the mid and lower troposphere, whereas land-based PCCs have higher regional differences among themselves, and they are more intense compared to oceanic-based PCCs. To attribute the atmospheric environment for intense PCCs, we investigated a few convective parameters during two seasons using NCEP & ECMWF reanalysis data and discussed below. CAPE values represent the updraft speed; however, both variables do not show any direct relationship (e.g., Yuter & Houze, 1995; Zipser, 2003). CAPE value depends on the air temperature (T) and specific humidity (q), and a higher CAPE favors the deep convection (Wu et al. 2020). Figure 15 is showing the mean value of CAPE (a-b), mean T (c-d) and mean q (e–f) during the JJAS and DJFM months for the year between 2014 and 2021. It is observed that CAPE is higher over the areas, where T and q are higher, but CAPE mostly follows the q patterns. The Spatial distribution of mean CAPE is consistent with the frequency occurrences of CbTs and ICC8s but not the ICC3s (Fig. 1). The atmospheric T is higher over the continental areas during both the seasons, which is also responsible for the large sensible flux over the land compared to oceans (Fig. 15c–d). However, the position of maximum air T shifts from the northern latitude to the southern latitude from JJAS months to DJFM months. During the JJAS months the maximum T is observed over the Indian continent (especially near WHF), Indo-China Peninsula and Africa. We also observed several wet spots ($q > 20$ gkg^{-1}), which are mostly concentrated over the ITCZ (Intertropical Convergence Zone). Tropical Indian Ocean, Bay of Bengal and tropical west Pacific Ocean also show the higher q (Fig. 15e–f). But at the same time, the mid-latitude continent shows the less q in the northern and southern hemisphere. q shows the different characteristics during the DJFM months, and wet spots ($q > 20$ g kg^{-1}) were observed at the southern latitude and central/eastern Pacific Ocean. Wet spots also penetrated over the continent areas of SA and north Australia. The locations of higher T and q match with the fewer locations of deeper and intense convection but not true for all the cases.

Moist static energy (MSE) plays a vital role in deep convection (Sherwood et al., 2004). Figure 16 shows the surface MSE during the two seasons (Fig. 16a: JJAS and Fig. 16b: DJFM) and vertical profiles of MSE (Fig. 16c) over the selected areas. Surface MSE shows that tropical areas have higher surface MSE during both the seasons and reduces gradually at higher latitudes. Higher surface MSE values are matching with the locations of higher frequency of PCCs. However, the vertical profiles of MSE show some interesting features. For example, all the land-dominated regions are showing the higher MSE in the mid and upper troposphere except over SDC. The higher MSE over land-dominated areas are more consistent with the intensity and depth of the PCCs in the northern hemisphere. IGP and WHF have higher MSE and correspond to intense and deep

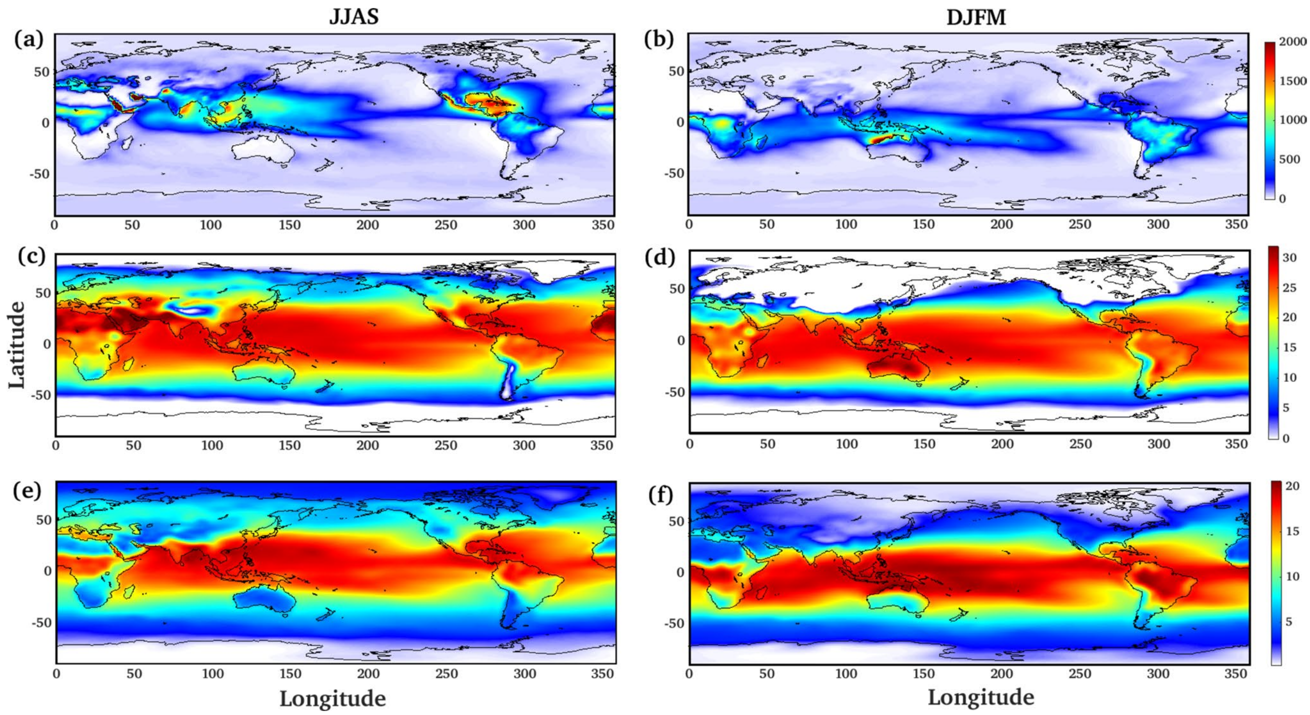

Fig. 15 Spatial distribution of **a** convective available potential energy: JJAS; **b** convective available potential energy: DJFM; **c** surface temperature: JJAS; **d** surface temperature: DJFM; **e** specific humidity: JJAS; **f** specific humidity: DJFM; during study periods

precipitating cloud cells. However, SDC has the least MSE and gains the MSE at the upper level, but they also have the most intense PCCs. Among the tropical oceanic areas, BOB (AO) has the highest (least) MSE in the mid-troposphere and they have the most intense (least intense) PCCs.

The most intense PCCs are observed over subtropical areas, namely at WHF and SDC during JJAS and DJFM months, respectively (Houze et al., 2007; Kumar & Bhat, 2016; Zipser et al., 2006), although their frequencies are less (Fig. 3; Table 1). It reflects that these regions do not produce frequent convection and rainfall (Fig. 1), but whenever they do, it could be very intense (Table 1). The possible reason behind such behavior is well-known capping inversion mechanisms, which are the results of geographical locations and surface flux feedback (Houze et al., 2007; Medina et al., 2010). Basically, the moist and warm air from the oceanic flow is capped by the continental dry and cold air mass from the mid-latitude and caps atmospheric instability within the stable layer. The intense convection will result only when an orographically induced unstable flow releases the instability. AO has a higher concentration of small-sized hydrometeors and the weakest vertical profiles among all the selected areas. The lower vertical velocity restricts the hydrometeors to move deeper into the upper atmosphere and reveals that most of the precipitation are coming from the shallow clouds (Heymsfield et al., 2010; Kumar, 2018; Zipser & Lutz, 1994).

The vertical depth and intensity of hydrometeors is the result of cloud dynamics and microphysical processes. For example, low-level convergence, vertical velocity and wind shear influence the precipitation near the small mountain regions (Lasher Trapp et al., 2018; Flores-Rojas et al. 2019a, b). The peaks in Z_e and D_m are observed between 3 and 5 km, and then they decrease as altitude increases; however, the slope is different in different cloud cells. The vertical profiles (Z_e and DSD) depend on several environmental factors such as temperature and humidity structure. Also, the cloud microphysical processes affect the hydrometeors size and concentration and then affect the vertical profiles. These microphysical processes depend on environmental factors (Zipser & Lutz, 1994; Heymsfield et al., 2010) and explained earlier too. However, after seeing with different climatic conditions so many factors we can say that specific-based locations, geographic features, local wind pattern and orography play a major role in deep and intense convection and DSD parameters and must be investigated in the future on the individual case basis.

The major findings are mentioned below:

1. The regional differences in the average vertical profiles of PCCs are very less among the different tropical oceanic areas. However, of all the oceanic-dominated areas, the Maritime Continent and the Bay of Bengal have the most intense PCCs.

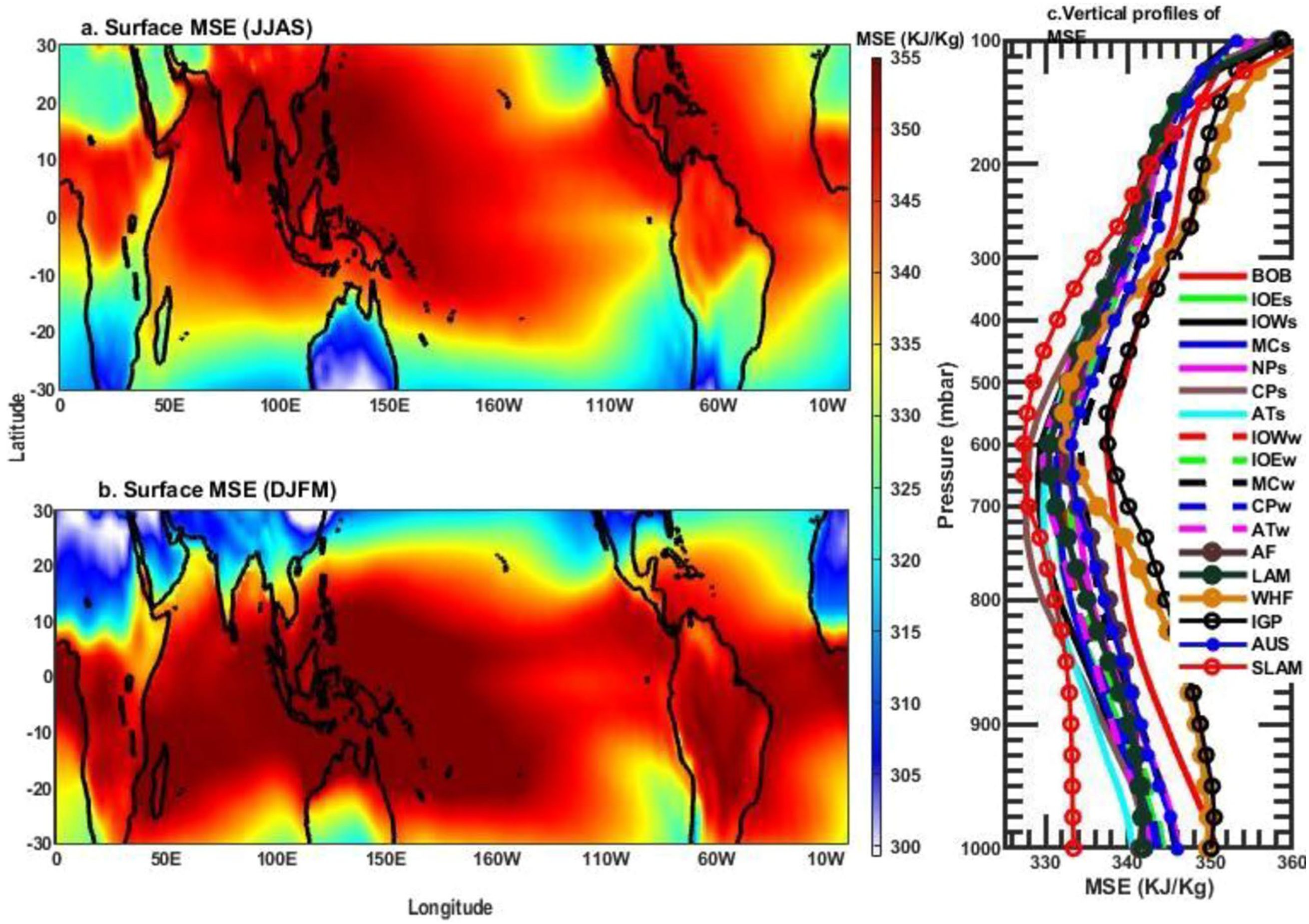

Fig. 16 Surface moist static energy during **a** JJAS and **b** DJFM months for the years between 2014 and 2021. Average vertical profiles of moist static energy over the selected areas

2. The most intense PCCs are observed over Western Himalaya Foothills and Sierra De Cordoba during JJAS and DJFM months, respectively, although their frequencies are less. North Australia has the least intense PCCs during DJFM months among all the land-dominated regions.
3. The hydrometeors size (D_m) and concentration (N_w) show the opposite characteristics with the PCCs intensity. For example, the most intense PCCs of WHF and SDC consist of the highest size of hydrometeors among all the selected areas. However, weak intense cloud cells show the opposite characteristics and weak cloud cells consist of higher concentrations (N_w) of small-sized hydrometeors (D_m).
4. Spatial distribution among the land and oceanic-based PCCs reveals that land areas consist of larger hydrometeors (D_m) and differences in D_m are higher at 3 km altitude compared to 8 km altitude. The average profiles show that regional differences are higher in mixed phase altitude.
5. The two-dimensional joint histogram of altitudinal variation in D_m shows the two modes in D_m at 1 and > 3 mm, whereas oceanic regions only show one mode nearly at 1 mm.

One of the biggest challenge in meteorology is the correct estimation of the amount of the rainfall falling on the Earth's surface. The quantity preliminary depends on the DSD parameters near the surface and how they vary regionally with the altitude in various types of vertically developed clouds. This is an attempt to quantify them and in the future information about the climatological variation of DSD parameters over specific locations will improve their representation in the climate models (Xu & Zipser, 2012).

Acknowledgements GPM Data (GES DISC DATASET: GPM DPR KU PRECIPITATION PROFILE 2A 1.5 HOURS 5 KM V07 (GPM_2AKU 07) (NASA.GOV)) and 3B42 (http://mirador.gsfc.nasa.gov/cgi-bin/ mirador/presentNavigation.pl?tree=project&dataset=3B42:%203-Hour%200.25%20x%200.25%20degree% 20merged%20 TRMM%20and%20other%20satellite% 20estimates&project=TRMM

&dataGroup=Gridded& version=007) data are taken from NASA's Earth–Sun System Division website. The authors thank the anonymous reviewers for their constructive suggestions. TMI data were produced by Remote Sensing Systems, Inc., and were sponsored by the NASA Earth Sciences Division.

Author Contributions SK helped in conceptualization, validation, methodology, data analysis, radar data concept, algorithm development and wrote the original draft; JLF was involved in data collection and edited the original draft; DM helped in concept and edited the manuscript; ASM edited the manuscript; YSV edited the manuscript. All authors have read and agreed to the published version of the manuscript.

Funding No funding was received.

Declarations

Conflict of interest The authors declared that they have no conflict of interest.

References

Bhat, G. S., & Kumar, S. (2015). Vertical structure of cumulonimbus towers and intense convective clouds over the South Asian region during the summer monsoon season. *Journal of Geophysical Research: Atmospheres, 120*, 1710–1722.

Cetrone, J., & Houze Jr, R. A. (2009). Anvil clouds of tropical mesoscale convective systems in monsoon regions. *Quarterly Journal of the Royal Meteorological Society: A Journal of the Atmospheric Sciences, Applied Meteorology and Physical Oceanography*, *135*(639), 305–317.

Das, S., & Maitra, A. (2016). Vertical profile of rain: Ka band radar observations at tropical locations. *Journal of Hydrology*, *534*, 31–41. https://doi.org/10.1016/j.jhydrol.2015.12.053

Del Castillo-Velarde, C., Kumar, S., Valdivia-Prado, J. M., Moya-Álvarez, A. S., Flores-Rojas, J. L., & Villalobos-Puma, E. (2021). Evaluation of GPM dual-frequency precipitation radar algorithms to estimate drop size distribution parameters, using ground-based measurement over the central Andes of Peru. *Earth Systems and Environment*, *5*, 597–619.

Dee, D. P., et al. (2011). The ERA-Interim reanalysis: Con"guration and performance of the data assimilation system. *Quarterly Journal Royal Meteorological Society, 137*, 553–597.

Fabry, F., & Zawadzki, I. (1995). Long-term radar observations of the melting layer of precipitation and their interpretation. *Journal of the Atmospheric Sciences, 52*, 838–851.

Flores-Rojas, J. L., Cuxart, J., Piñas-Laura, M., Callañaupa, S., Suárez-Salas, L., & Kumar, S. (2019a). Seasonal and diurnal cycles of surface boundary layer and energy balance in the central andes of peru, mantaro valley. *Atmosphere*, *10*(12), 779.

Flores Rojas, J. L., Moya-Alvarez, A. S., Kumar, S., Martínez-Castro, D., Villalobos-Puma, E., & Silva-Vidal, Y. (2019b). Analysis of possible triggering mechanisms of severe thunderstorms in the tropical central Andes of Peru, Mantaro Valley. *Atmosphere*, *10*(6), 301.

Hamada, A., & Takayabu, Y. N. (2016). Improvements in detection of light precipitation with the global precipitation measurement dual-frequency precipitation radar (GPM DPR). *Journal of Atmospheric and Oceanic Technology*, *33*(4), 653–667.

Heymsfield, G. M., Tian, L., Heymsfield, A. J., Li, L., & Guimond, S. (2010). Characteristics of deep tropical and subtropical convection from nadir-viewing high–altitude airborne doppler radar. *Journal of the Atmospheric Sciences, 67*, 285–308.

Hirose, M., & Nakamura, K. (2005). Spatial and diurnal variation of precipitation systems over Asia observed by the TRMM precipitation radar. *Journal of Geophysical Research, 110*, D05106. https://doi.org/10.1029/2004JD004815

Hou, A. Y., Kakar, R. K., Neeck, S., Azarbarzin, A. A., Kummerow, C. D., Kojima, M., Oki, R., Nakamura, K., & Iguchi, T. (2014). The global precipitation measurement mission. *Bulletin of the American Meteorological Society, 95*, 701–722.

Houze, R. A., Jr. (1993). *Cloud dynamics*. Academic Press.

Houze, R. A. (2012). Orographic effects on precipitating clouds. *Reviews of Geophysics, 50*(RG1001), 47. https://doi.org/10.1029/2011RG000365

Houze, R. A., Jr., Wilton, D. C., & Smull, F. B. (2007ba). Monsoon Convection in the Himalayan Region as Seen by the TRMM Precipitation Radar. *Quarterly Journal of the Royal Meteorological Society, 133*, 1389–1411.

Kalnay, E., et al. (1996). The NCEP/NCAR 40 year reanalysis project. *Bulletin of the American Meteorological Society, 77*, 437–470.

Kumar, S. (2023). Regional and seasonal differences of radar reflectivity slopes in lower troposphere in convective and stratiform precipitation using TRMM PR data. *Theoretical and Applied Climatology*, 1–10.

Kumar, S., & Bhat, G. S. (2019). Frequency of a state of cloud systems over tropical warm ocean. *Environmental Research Communications, 1*(6), 061003.

Kumar, S., & Silva, Y. (2019). Vertical characteristics of radar reflectivity and DSD parameters in intense convective clouds Over South East South Asia during Indian summer monsoon. *International Journal of Remote Sensing, 40*, 9604–9628. https://doi.org/10.1080/01431161.2019.1633705

Kumar, S. (2016). Three dimensional characteristics of precipitating cloud systems observed during Indian summer monsoon. *Advances in Space Research, 58*(6), 1017–1032. https://doi.org/10.1016/j.asr.2016.05.052

Kumar, S. (2017a). A 10-year climatology of vertical properties of most active convective clouds over the Indian regions using TRMM PR. *Theoretical and Applied Climatology, 127*(1–2), 429–440. https://doi.org/10.1007/s00704-015-1641-5

Kumar, S. (2017b). Vertical characteristics of reflectivity in intense convective clouds using TRMMPR data. *Environment and Natural Resources Research, 7*(2), 58. https://doi.org/10.5539/enrr.v7n2p58

Kumar, S. (2018). Vertical structure of precipitating shallow echoes observed from TRMM during Indian summer monsoon. *Theoretical and Applied Climatology, 133*(3–4), 1051–1059. https://doi.org/10.1007/s00704-017-2238-y

Kumar, S., & Bhat, G. S. (2016). Vertical profiles of radar reflectivty factor in intense convective clouds in the tropics. *Journal of Applied Meteorology and Climatology, 55*(5), 1277–1286. https://doi.org/10.1175/JAMC-D-15-0110.1

Kumar, S., & Bhat, G. S. (2017). Vertical structure of orographic precipitating clouds observed over South Asia during summer monsoon season. *Journal of Earth System Science, 126*(8), 114. https://doi.org/10.1007/s12040-017-0897-9

Kumar, S., Castillo-Velarde, C. D., Flores Rojas, J. L., Moya-Álvarez, A., Martínez Castro, D., Srivastava, S., & Silva, Y. (2020a). Precipitation structure during various phases the life cycle of precipitating cloud systems using geostationary satellite and space-based precipitation radar over Peru. *Giscience & Remote Sensing, 57*(8), 1057–1082. https://doi.org/10.1080/15481603.2020.1843846

Kumar, S., Castro, C., Moya-Álvarez, A. S., Martínez-Castro, D., & Silva-Vidal, Y. (2020b). Effect of South American low level flow and andes mountain on the tropical and mid latitude precipitating cloud systems: GPM observations. *Theoretical and Applied Climatology, 141*, 157–172. https://doi.org/10.1007/s00704-020-03155-x

Kumar, S., Castro, C., Valdivia, J. H., Rojas, J. F. L., MagalyCallanaupa, S., Silva-Vidal, Y., Moya-Álvarez, A. S., & Martínez-Castro, D. (2020c). Rainfall characteristics in the Central Andes of Peru from a vertically pointed profile rain radar and in-situ field Campaign. *Atmosphere, 11*, 248. https://doi.org/10.3390/atmos11030248

Kumar, S., & Silva, Y. (2020). Distribution of hydrometeors in intense convective clouds over South America during austral summer monsoon seasons: GPM observations. *International Journal of Remote Sensing, 41*, 3677–3707. https://doi.org/10.1080/01431161.2019.1707899

Kumar, S., Flores, J. L., Moya-Álvarez, A. S., Martinez-Castro, D., & Silva, Y. (2023). Characteristics of cloud properties over South America and over Andes observed using CloudSat and reanalysis data. *International Journal of Remote Sensing*, *44*(6), 1976–2004.

Kumar, S., Silva-Vidal, Y., Moya-Álvarez, A. S., & Martínez-Castro, D. (2019a). Effect of the surface wind flow and topography on precipitating cloud systems over the andes and associated Amazon Basin: GPM observations. *Atmospheric Research, 225*, 193–208. https://doi.org/10.1016/j.atmosres.2019.03.027

Kumar, S., Silva-Vidal, Y., Moya-Álvarez, A. S., & Martínez-Castro, D. (2019b). Seasonal and regional differences in extreme rainfall events and their contribution to the world's precipitation: GPM observations: GPM observations. *Advances in Meteorology, 2019*, 1–15. https://doi.org/10.1155/2019/4631609

Kumar, S., & Srivastava, S. (2022). A vertical characteristics of precipitating cloud systems during different phases of life cycle of cloud systems using satellite-based radar over tropical Oceanic areas. *Journal of Applied and Natural Science, 14*(4), 1272–1285. https://doi.org/10.31018/jans.v14i4.3691

Lasher-Trapp, S., Kumar, S., Moser, D. H., Blyth, A. M., French, J. R., Jackson, R. C., Leon, D. C., & Plummer, D. M. (2018). On different microphysical pathways to convective rainfall. *Journal of Applied Meteorology and Climatology, 57*(10), 2399–2417. https://doi.org/10.1175/JAMC-D-18-0041.1

Lavanya S., Kirankumar, N. V. P., Aneesh, S., Subrahmanyam, K. V., & Sijikumar, S. (2019). Seasonal variation of raindrop size distribution over a coastal station Thumba: A quantitative analysis. *Atmospheric Research*. https://doi.org/10.1016/j.atmosres.2019.06.004

Li, W., & Schumacher, C. (2011). Thick anvils as viewed by the TRMM precipitation radar. *Journal of Climate, 24*, 1718–1735.

Liu, C., & Zipser, E. J. (2015). The global distribution of largest, deepest, and most intense precipitation systems. *Geophysical Research Letters*, *42*(9), 3591–3595.

Liu, C., Zipser, E. J., Cecil, D. J., Nesbitt, S. W., & Sherwood, S. (2008). A cloud and precipitation feature database from nine years of TRMM observations. *Journal of Applied Meteorology and Climatology, 47*(10), 2712–2728. https://doi.org/10.1175/2008JAMC1890.1

Lucas, C., Zipser, E. J., & LeMone, M. A. (1994ba). Vertical velocity in oceanic convection off tropical Australia. *Journal of Atmospheric Science, 51*, 3183–3193.

Medina, S., Houze, R. A., Jr., Kumar, A., & Niyogi, D. (2010). Summer monsoon convection in the Himalayan region: Terrain and land cover effects. *Quarterly Journal of the Royal Meteorological Society, 136*, 593–616.

Nesbitt, S. W., Cifelli, R., & Rutledge, S. A. (2006). Storm morphology and rainfall characteristics of TRMM precipitation features. *Monthly Weather Review, 134*, 2702–2721.

Nesbitt, S. W., Zipser, E. J., & Cecil, D. J. (2000). A census of precipitation features in the tropics using TRMM radar, ice scattering, and lightning observations. *Journal of Climate, 13*, 4087–4106.

Petersen, W. A., & Rutledge, S. A. (2001). Regional variability in tropical convection: Observation from TRMM. *Journal of Climate, 13*, 4087–4106.

Qie, X. S., Wu, X. K., Yuan, T., Bian, J. C., & Lu, D. R. (2014). Comprehensive pattern of deep convective systems over the Tibetan Plateau-South Asian monsoon region based on TRMM data. *Journal of Climate, 27*, 6612–6626. https://doi.org/10.1175/JCLI-D-14-00076.1

Riehl, H., & Malkus, J. S. (1958). On the heat balance in the equatorial trough zone. *Geophysica, 6*, 503–538.

Romatschke, U., Medina, S., & Houze, R. A., Jr. (2010). Regional, seasonal, and diurnal variations of extreme convection in South Asian region. *Journal of Climate, 23*, 419–439.

Sherwood, S. C., Minnis, P., & McGill, M. (2004). Deep convective cloud-top heights and their thermodynamic control during crystalface. *Journal of Geophysical Research: Atmospheres*. https://doi.org/10.1029/2004JD004811

Stith, J. L., Dye, J. E., Bansemer, A., Heymsfield, A. J., Grainger, C. A., Petersen, W. A., & Cifelli, R. (2002). Microphysical observations of tropical clouds. *Journal of Applied Meteorology, 41*, 97–117.

Takayabu, Y. N. (2002). Spectral representation of rain profille and diurnal variations observed with TRMM PR over the equatorial area. *Geophysical Research Letters, 29*(12), 1584. https://doi.org/10.1029/2001GL014113

Williams, E. R., Weber, M. E., & Orville, R. E. (1989). The relationship between lightning type and convective state of thunderclouds. *Journal of Geophysical Research, 94*, 13213–13220.

Wu, X., Qie, X., & Yuan, T. (2013). Regional distribution and diurnal variation of deep convective systems over the Asian monsoon region. *Science China Earth Sciences*, *56*, 843–854.

Wu, X., Qie, X., Yuan, T., & Li, J. (2016). Meteorological regimes of the most intense convective systems along the southern Himalayan front. *Journal of Climate*, *29*(12), 4383–4398.

Wu, X., Yuan, T., Qie, K., & Luo, J. (2020). Geographical distribution of extreme deep and intense convective storms on Earth. *Atmospheric Research*, *235*, 104789.

Xu, W., & Zipser, E. J. (2012). Properties of deep convection in tropical continental, monsoon, and oceanic rainfall regimes. *Geophysical Research Letters, 39*, L07802.

Yuan, T., & Qie, X. (2008). Study on lightning activity and precipitation characteristics before and after the onset of the South China sea summer monsoon. *Journal of Geophysical Research, 113*, D14101.

Yuter, S. E., & Houze, R. A., Jr. (1995). Three-dimensional kinematic and microphysical evolution of Florida cumulonimbus: Part II. Frequency distribution of vertical velocity, reflectivity, and the differential reflectivity. *Monthly Weather Review, 123*, 1941–1963.

Zipser, E. J. (2003). Some views on "hot towers" after 50 years of tropical field programs and two years of TRMM data. In: W. K. Tao, & R. Adler (Eds.), *Cloud systems, hurricanes, and the tropical rainfall measuring mission (TRMM). Meteorological Monographs* (Vol. 51, pp. 49–58). Boston, MA: American Meteorological Society.

Zipser, E. J., Cecil, D. J., Liu, C., Nesbitt, S. W., & Yorty, D. P. (2006). Where are the most intense thunderstorms on earth? *Bulletin of the American Meteorological Society, 87*, 1057–1071.

Zipser, E. J., & Lutz, K. R. (1994). The vertical profile of radar reflectivity of convective cells: A strong indicator of storm intensity and lightning probability? *Monthly Weather Review, 122*, 1751–1759.